IMSAR
International Maritime Studies and Research

journal homepage: https://dergipark.org.tr/en/pub/imsar

Modeling of a scaled-down sea vessel's gyrostabilizer for initial stabilization tests

Mehmet İsmet Can Dede[1*], Muhammed Rıza Bozelli[1], Berk Kurt[1] and Tolga Cankurt[1,2]

[1] Department of Mechanical Engineering, Izmir Institute of Technology, Izmir, Türkiye
[2] Hidropar Motion Control Technology Center Inc., İstanbul, Türkiye

[*] Corresponding author
E-mail address: candede@iyte.edu.tr

https://doi.org/10.5281/zenodo.17037008
Received 08 July 2025
Accepted for publication 28 August 2025
Published 09 September 2025

Abstract

Gyrostabilizers are employed to stabilize the roll motion of sea vessels. A test system for validating the working scheme of the gyrostabilizer and refining its control algorithms has been developed. This paper presents a mathematical model of this test system for the vessel and its gyrostabilizer system. This dynamic model is later evaluated against the simulation model developed via MATLAB Multibody blocks. The results validate the developed mathematical model, which can be used for controller development in future studies.

Keywords: Gyrostabilizer, Sea vessel stabilization, Dynamic modeling of gyrostabilizers

1. Introduction

Sea vessels are vehicles that use the buoyancy of water. In a general rigid-body-based approach, sea vessels have six degrees of freedom (DoF) in water. The translation motions about the x, y, and z axes are named as Surge, Sway, and Heave motions, respectively. Similarly, the rotational motions about the x, y, and z axes are named as Roll, Pitch, and Yaw motions, respectively. It is possible to describe a 6-DoF equation of a model for a ship as described in Equation 1 (Berghal, 2009).

$$\widehat{M}_s\ddot{\bar{\eta}} = \bar{F} \tag{1}$$

In Equation 1, M_s is a 6x6 mass matrix, $\bar{\eta}$ is a vector of position in the 6-DoF defined as $\bar{\eta} = (\eta_1, \eta_2, \eta_3, \eta_4, \eta_5, \eta_6)^{T,}$ and finally $\bar{F}$ represents the vector of forces and moments acting on the body,

which is defined as $\bar{F} = (F_1, F_2, F_3, M_1, M_2, M_3)^T$. The subscript on vectors of position, force, and moments represents the motion direction of the ship. The position (η_i) represents the respective motion in the direction of $i = 1,2,3,4,5,6$; surge, sway, heave, roll, pitch, and yaw, respectively. The force (F_i) and moment (M_i) represent the acting axis for $i = 1,2,3$; surge, sway, and heave. By differentiation of the position vector twice, the acceleration vector $(\ddot{\bar{\eta}})$ is obtained.

The mass matrix (M_s) has a structure as shown in Equation 2.

$$\widehat{M}_s = \begin{bmatrix} m & 0 & 0 & 0 & mz_G & 0 \\ 0 & m & 0 & -mz_G & 0 & 0 \\ 0 & 0 & m & 0 & 0 & 0 \\ 0 & -mz_G & 0 & I_{44} & 0 & -D_{46} \\ mz_G & 0 & 0 & 0 & I_{55} & 0 \\ 0 & 0 & 0 & -D_{46} & 0 & I_{66} \end{bmatrix} \tag{2}$$

In the mass matrix representation, m is the mass of the ship, z_g is the vertical component of the ship's mass center. The moment of inertia terms about the x, y, and z axes are represented as I_{44}, I_{55} and I_{66} respectively. Finally, D_{46} and D_{64} show the off-diagonal elements of the mass moment of inertia, and these parameters are significantly small due to the symmetric mass distribution of the vessel.

The force vector, $\bar{F}$, consists of three parameters as (1) the wave-exited forces (τ_ω), (2) the hydrodynamic reaction forces (τ_r) and (3) the reaction forces from the mooring system (τ_{rs}). If the ship is not tied to the shore at any point, this term becomes zero $(\tau_{rs} = 0)$. The wave-exited forces depend on the sea conditions. The remaining hydrodynamic reaction forces can be written as a function of the position vector of the ship.

$$\overline{\mathrm{T}}_{\mathrm{r}} = -\hat{A}_s\ddot{\bar{\eta}} - \hat{B}_s\dot{\bar{\eta}} - \hat{C}_s\bar{\eta} \tag{3}$$

In Equation 3, $\hat{A}_s$ is the added mass (hydrodynamic mass), $\hat{B}_s$ is the hydrodynamic damping, and finally $\hat{C}_s$ is the hydrostatic stiffness (hydrodynamic restoring). These matrices represent the characteristics of the sea vessel with 6x6 matrices as described in Equations 4, 5, and 6.

$$\hat{A}_s = \begin{bmatrix} A_{11} & 0 & 0 & 0 & A_{15} & 0 \\ 0 & A_{22} & 0 & A_{24} & 0 & 0 \\ 0 & 0 & A_{33} & 0 & 0 & 0 \\ 0 & A_{42} & 0 & A_{44} & 0 & 0 \\ A_{51} & 0 & 0 & 0 & A_{55} & 0 \\ 0 & 0 & 0 & 0 & 0 & A_{66} \end{bmatrix} \tag{4}$$

$$\hat{B}_s = \begin{bmatrix} B_{11} & 0 & 0 & 0 & B_{15} & 0 \\ 0 & B_{22} & 0 & B_{24} & 0 & 0 \\ 0 & 0 & B_{33} & 0 & 0 & 0 \\ 0 & B_{42} & 0 & B_{44} & 0 & 0 \\ B_{51} & 0 & 0 & 0 & B_{55} & 0 \\ 0 & 0 & 0 & 0 & 0 & B_{66} \end{bmatrix} \tag{5}$$

$$\hat{C}_s = \begin{bmatrix} 0 & 0 & 0 & 0 & 0 & 0 \\ 0 & 0 & 0 & 0 & 0 & 0 \\ 0 & 0 & C_{33} & 0 & C_{53} & 0 \\ 0 & 0 & 0 & C_{44} & 0 & 0 \\ 0 & 0 & C_{53} & 0 & C_{55} & 0 \\ 0 & 0 & 0 & 0 & 0 & 0 \end{bmatrix} \tag{6}$$

In the given mathematical expressions for A_{ij}, B_{ij} and C_{ij}, they have the form of hydrodynamic reactions i that are caused by motion in the direction j. Finally, the 6-DoF linear equation of motion of the ship is described in Equation 7.

$$\bar{\tau}_\omega = (\hat{M}_s + \hat{A}_s)\ddot{\bar{\eta}} + \hat{B}_s\dot{\bar{\eta}} + \hat{C}_s\bar{\eta} \tag{7}$$

Although the 6-DoF model of a ship may be useful for general applications, it may pose over complexity when studying roll stabilization systems. Marine vessels have a narrow structure along the travel direction to reduce the hydraulic friction at the keel part of the vessel. Although this structure effectively increases the performance of the vessel, it makes it more sensitive to rolling motion. Rolling motion is a crucial problem in the design of a ship because it determines the stability characteristics of a ship (Kornev, 2012). For these reasons, the policy makers, such as the International Maritime Organization (IMO), define the Intact Stability for the different kinds of sea vessels.

The acting forces on a sea vessel should be put forth when establishing a mathematical model for the rolling motion of a ship. Two types of forces act on the ship in the static equilibrium position: (1) inertial forces and (2) buoyancy forces. For static equilibrium, these two forces have to be equal. The gravitational acceleration results in a force that acts on the center of mass (G) in the downward direction. In turn, the submerged volume of the vessel generates an upward buoyancy force that acts on the buoyancy center (B) as shown in Figure 1.

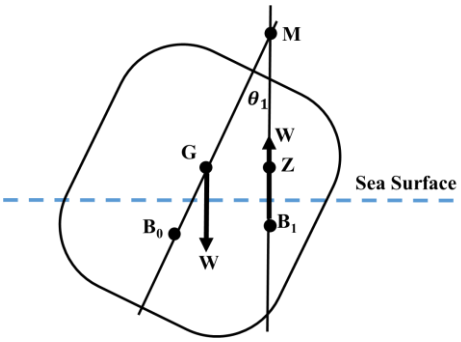

Figure 1. Free body diagram of the ship's rolling motion

The center of mass (G) and the center of buoyancy before the ship starts to roll B_0, and after the ship has rolled by θ_1 angle B_1 are shown in Figure 1. The center of buoyancy varies with the roll angle θ_1 of the ship, while the center of mass changes by adding or removing weight. The change of the other two parameters that appear in Figure 1, metacenter and z-point, are shown in Figure 2. Metacenter is an imaginary point used to describe the stability of the ship. The metacenter is the intersection of two lines passing through the center of mass and the center of buoyancy. The line passing through the center of mass is drawn parallel to the symmetry axes of the boat, while the other line passing through the center of buoyancy is drawn parallel to the gravity vector. Finally, Z is an imaginary point located on the MB_1 line.

The distance defined by $\left|\overrightarrow{GZ}\right| = GZ$ (righting arm) and the buoyancy force generates the righting moment about the center of mass.

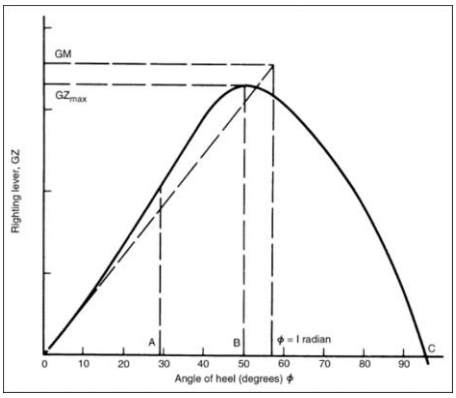

Figure 2. Static stability curve / gz curve of a ship (Chakraborty, 2022)

Figure 2 shows the static stability curve of a sea vessel. The x-axis indicates the roll angle (heel angle $\phi = \theta_1$) while the y-axis indicates the righting lever or the distance GZ. The righting lever is a non-linear property of the ship. However, the righting lever shows linear characteristics up to $\phi = 15°$. The righting lever magnitude increases up to $50°$and then suddenly decreases as the roll angle increases. This is significant when considering the capsizing of sea vessels. After a roll angle, the system cannot generate enough righting moment to recover the ship, and the ship overturns. The metacentric height (GM) is the distance between the metacenter M and the center of mass G of the ship. It is a powerful tool for describing the stability of the ship. By investigating the geometry generated by $G - Z - M$ points, as can be depicted in Figure 1, Equation 8 can be derived (Ibrahim and Grace, 2010).

$$GMsin(\theta_1) = GZ \tag{8}$$

By considering the small angle approximation, $\sin(\theta_1) \approx \theta_1$, the righting arm can be expressed as a function of roll angle. Since the buoyancy force is equal to the weight of the ship, the righting moment (heeling moment) can be expressed as a function of roll angle (Ibrahim and Grace, 2010) as follows:

$$M_R = g\rho\nabla GM\theta_1 \tag{9}$$

In Equation 9, g is the gravity constant $[m/s^2]$, ρ is the density of water $[kg/m^3]$, ∇ is the displacement of the ship $[m^3]$ and M_R is the righting moment of the ship $[Nm]$. However, Equation 9 is only valid for small angles (i.e., up to $15°$). For more comprehensive mathematical models, the GZ curve must be considered.

Considering the information about a ship's roll motion and the metacenter point calculations, a pendulum system is chosen to simulate the ship's motion around the constant metacenter point for small roll angles. This selection enables the establishment of an initial scaled-down test system for the purpose of defining the ship's equation of motion, considering only the roll motion.

Once the conceptual design with the constant metacenter is determined, the free-body diagrams (FBD) of the system are created. The FBDs include information such as the axes of motion, distances between joint points, and the center of mass, which are processed parametrically. A comprehensive kinematic and dynamic analysis of the system is conducted by utilizing the aforementioned parameters.

To validate the kinematics and dynamics analyses, the three-dimensional design of the system is developed in a computer-aided-design (CAD) software and transferred to the MATLAB Simulink simulation environment in terms of a Multibody blocks-based model. The accuracy of dynamic calculations is verified by comparing the results with the simulation data, which incorporates the physical properties that are extracted from the CAD software. Using a MATLAB Multibody blocks-based model for the kinematics verification was previously studied by Dede (2024). In this work, verification is carried out using both kinematics and dynamics analyses. Before presenting the dynamic model of the gyrostabilizer, the sea state models and the state of the art in gyrostabilizer controllers are discussed in the next sections.

2. The Sea State Models

The marine environment is harsh and imposes highly dynamic conditions on sea vessels. Waves are complex phenomena due to their multi-source origin (e.g., tides, winds, currents, and seismic activity). Among these wave sources, tidal effects are predictable, occurring twice daily (Molland, 2011). On the other hand, wind-generated waves are more frequent and dominate the energy spectrum in marine conditions (Toffoli and Elzbieta, 2017).

Waves are often described by using parameters such as the significant wave height (H_s) and the mean wave period ($\bar{T}$). Based on these parameters, the classification of sea states is provided in Table 1 (Liu et al., 2018). These parameters are widely used for engineering applications (e.g., ship stability analyses, fatigue analysis, and development of offshore energy systems).

Table 1. The sea states and wave properties (Liu et al., 2018)

Sea States	$T\ [s]$	$H_s[m]$
1	2.0	0.09
2	4.8	0.67
3	6.5	1.40
4	8.1	2.44
5	9.7	3.66
6	11.3	5.49
7	13.6	9.14
8	17.0	15.24

The energy distribution of waves is represented by several spectral models, and the most widely implemented ones are the Pierson–Moskowitz (PM) spectrum (Pierson and Moskowitz, 1964; ITTC, 2002) and the JONSWAP spectrum (Hasselmann et al., 1973). The PM spectrum includes a model that represents a fully developed sea under steady wind conditions and is also referred to as the Bretschneider spectrum. In contrast, the JONSWAP spectrum introduces modifications to account for limited fetch and coastal effects, providing a more accurate representation of developing seas.

General formulations of these spectra define energy density as a function of frequency, with constants determined from parameters such as wind velocity, spectral peak frequency, or significant wave height (ITTC, 2002). Extensions of these models, including ISSC and ITTC spectra, refine the description further by incorporating mean frequencies and empirical coefficients.

$$S(f) = \frac{A}{f^2} \exp\left(-\frac{B}{f^4}\right) \tag{10}$$

The roll excitation of ships due to waves can be estimated by combining wave spectra with vessel hydrodynamic characteristics. In simplified form, the excitation moment spectrum is proportional to both the square of the wave slope spectrum and the restoring properties of the vessel (Olmez and Cakici, 2022). While frequency-domain spectra provide useful insights for analysis, time-domain simulations are often constructed by superposing harmonic components with random phases derived from the energy distribution function. The excitation moment spectrum can be calculated using the characteristic properties of the vessel, as expressed in Equation 11.

$$S_{F_{40}}(\omega) = (gmGM_t\omega^2)^2 S_{\beta\zeta}(\omega) \tag{11}$$

In the moment spectrum can be calculated using the characteristic properties of the vessel. Where g is the gravitational acceleration, m is the vessel mass, GM_t is the transverse metacentric height, ω is the wave frequency, and $S_{\beta\zeta}(\omega)$ is the wave slope spectrum.

The wave excitation moment spectrum can be used for initial investigation; however, it is not useful for simulation purposes. Therefore, the following equation can be used for generating a time domain signal by superposing the randomly selected frequency ω_n and the phase angle ψ_n for each selected frequency.

$$F_{ext}(t) = F_{40}(t) = \sum_{n=1}^{N\,freq} \sqrt{2\, S_{F_{40}}(\omega_n)\delta\omega}\, \cos(\omega_n t + \psi_n) \tag{12}$$

3. Gyrostabilizer Control Strategies

The concept of gyroscopic systems dates back to 1743, when the first proposal was for an artificial horizon. Their refinement and patents were obtained in the late 19th century, and by 1908, they were applied as gyrostabilizers. With the space race of the 1960s, gyroscopes became critical for spacecraft attitude control. More recently, the gyrostabilizers have found applications in renewable energy, such as wave energy systems (Townsend and Ramanand, 2011).

A gyrostabilizer consists of two primary parts: (1) a flywheel with high angular momentum $L = I \cdot \omega$ and (2) a gimbal that redirects this momentum. Gyrostabilizers are a subset of spinning-wheel devices, designed to dampen oscillatory motions. They can be classified by the number of gimbals (single or double) and their actuation strategy (passive or active). Multi-wheel configurations can generate multi-axis torques, though they are more complex to control (Townsend and Ramanand, 2011).

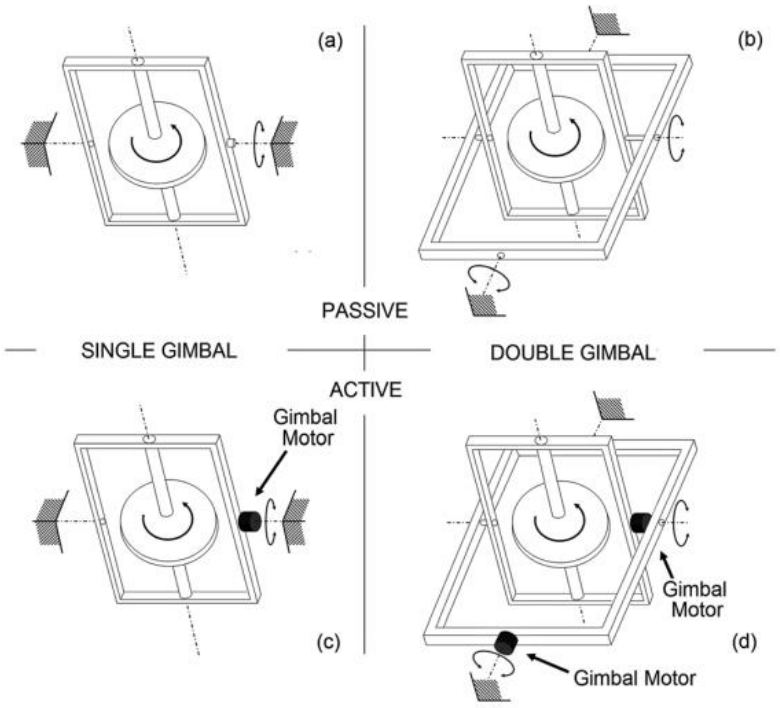

Figure 3. Motion types of spinning wheel (Source: Townsend and Ramanand, 2011)

Two main types are commonly used in marine applications: horizontal spin-axis and vertical spin-axis gyrostabilizers (Veem Marine, 2015). The vertical type has the advantage of passive control due to its natural equilibrium point, whereas the horizontal type requires active actuation. For this reason, commercial systems (e.g., Seakeeper, VEEM) typically employ vertical-axis designs. However, both systems face the singularity problem known as gimbal lock, where the spin axis aligns with the roll axis.

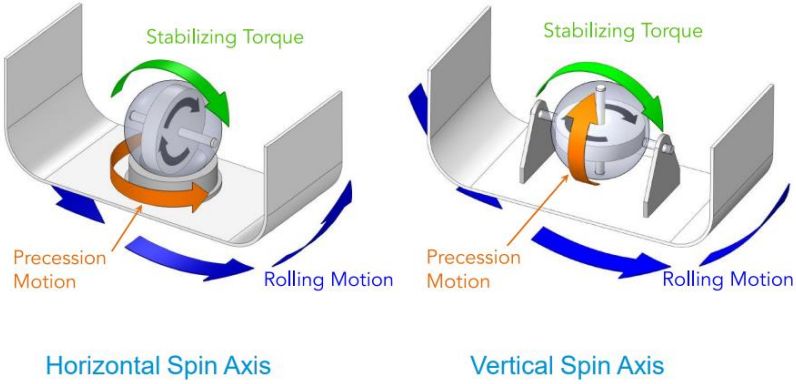

Figure 4. Horizontal and Vertical spin axis types of gyrostabilizers (Veem Marine, 2015)

The coupled dynamics of the ship and gyrostabilizer can be expressed as (Perez and Steinman, 2009):

$$I_{44}\ddot{\theta}_1 + B_{44}\dot{\theta}_1 + C_{44}\theta_1 = \tau_\omega - nK_g\dot{\theta}_2\cos(\theta_2) \tag{13}$$

$$I_g\ddot{\theta}_2 + B_g\dot{\theta}_2 + C_g\sin(\theta_2) = K_g\dot{\theta}_1\cos(\theta_2) + \tau_p \tag{14}$$

where I_{44}, B_{44}, C_{44} are the inertia, damping, and restoring coefficients of the ship, and I_g, B_g, C_g those of the gyrostabilizer. θ_1, θ_2 represent roll and precession motions, τ_ω the wave excitation, τ_p the control torque, K_g the angular momentum, and n the number of gyrostabilizers.

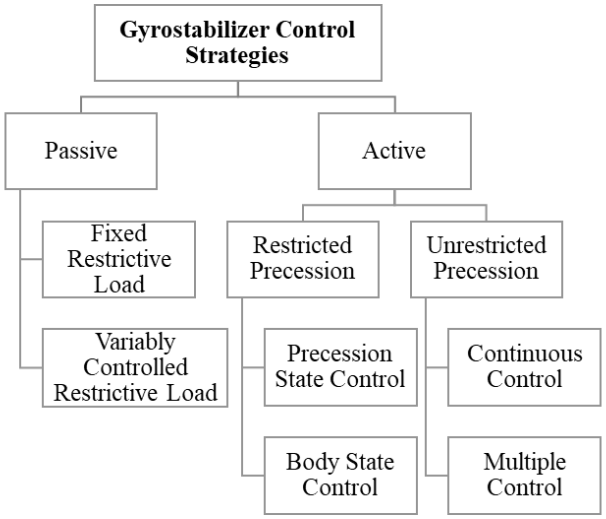

Figure 5. Gyrostabilizer control strategies (Townsend and Ramanand, 2011)

Control strategies are divided into passive and active. Passive control applies a constant or variable restrictive torque τ_g, but is inefficient. Active control regulates the precession rate using actuators. In body-state control, the precession rate is proportional to the ship's roll rate:

$$\dot{\theta}_2 = K_2 \dot{\theta}_1 \tag{15}$$

leading to an increased damping term in the ship's dynamics:

$$I_{44}\ddot{\theta}_1 + \left(B_{44} + nK_gK_2\right)\dot{\theta}_1 + C_{44}\theta_1 = \tau_\omega \tag{16}$$

Other advanced active control methods include precession-state control, singularity-robust strategies, extended Jacobian methods, and reaction wheel approaches (Townsend and Ramanand, 2011; Townsend and Shenoi, 2014). Their main objective is to mitigate singularity effects and improve system robustness.

Up to this section, ship roll dynamics, sea state models, and gyrostabilizer types with their control strategies are reviewed. Gyrostabilizers can be configured in various ways, influencing the choice of active or passive control. In this paper, a vertical spin-axis gyrostabilizer with active body-state control is studied. The next section provides the dynamic analyses for a scaled-down version of this type of gyrostabilizer.

4. The Dynamic Analyses of the Scaled-Down Gyrostabilizer Test System

The moving parts in the scaled-down gyrostabilizer test system consist of the ship (1), gyrostabilizer enclosure (2), and the flywheel (3). The ship part can perform only the roll motion. It rotates about a pivot point, which is considered the metacenter, thanks to a revolute joint. The enclosure part is a connection part that allows the gyrostabilizer to perform the precession movement. This part connects the flywheel and the ship, and its angular motion directly affects the magnitude of the counter-damping moment. Finally, the flywheel is connected to the enclosure with a rotary joint. The rotational speed of this part and

the mass moment of inertia on the axis of rotation form the angular momentum of the system. This generated angular momentum value, together with the precession rate, forms the anti-rolling torque of the system.

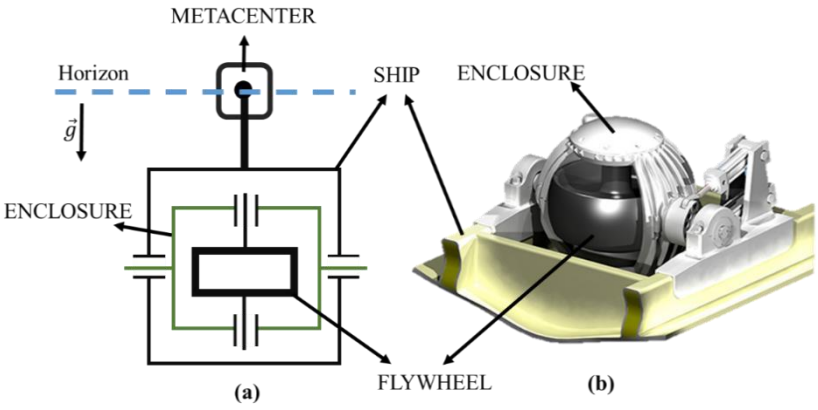

Figure 6. (a) The conceptual design of the gyrostabilizer system. (b) CAD of a gyrostabilizer system that is placed on a ship hull (Allied Motion, 2021)

Based on the kinematic sketch presented in Figure 6(a), dynamic analyses are carried out. Initially, the free-body diagrams of each part of the system are drawn as shown in Figures 7, 8, and 9. In these sketches, the center of mass of each part is defined as G_i, where $i = 1,2,3$. The subscript (i) is used to define which part it belongs to, namely the ship, enclosure, and flywheel, respectively. Additionally, the linear accelerations, angular accelerations, and angular velocities are defined as $\vec{a}_i$, $\vec{\alpha}_i$ and $\vec{\omega}_i$ respectively. The revolute joints' axis location is defined as O_i. The body-fixed coordinate system's axes are defined by unit vectors $\vec{u}_1^{(i)}$, $\vec{u}_2^{(i)}$ and $\vec{u}_3^{(i)}$. Subsequently, the rotation of the system's components is defined by θ_i. The positions of the pivot points and mass centers are defined as r_{ij} and g_{ij} where $i = 1,2,3$ and $j = 1,2,3$, respectively. Finally, the acting forces and torques on the bodies are defined as $\vec{F}_{ij}$ and $\vec{M}_{ij}$ denoting the force or moment imposed on a part j by part i.

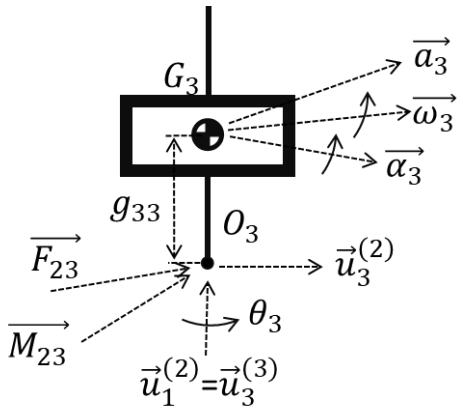

Figure 7. The free-body diagram of the flywheel

Once the parameters of the free-body diagrams have been defined, the kinematic analyses are performed to determine the linear acceleration, angular acceleration, and angular velocity of each mass center.

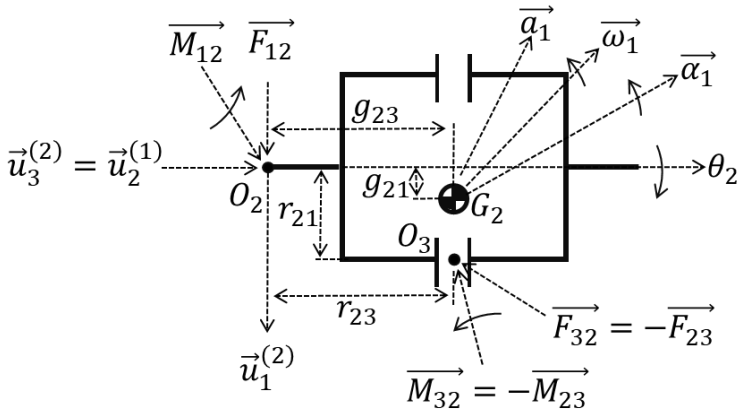

Figure 8. The free-body diagram of the gyrostabilizer enclosure

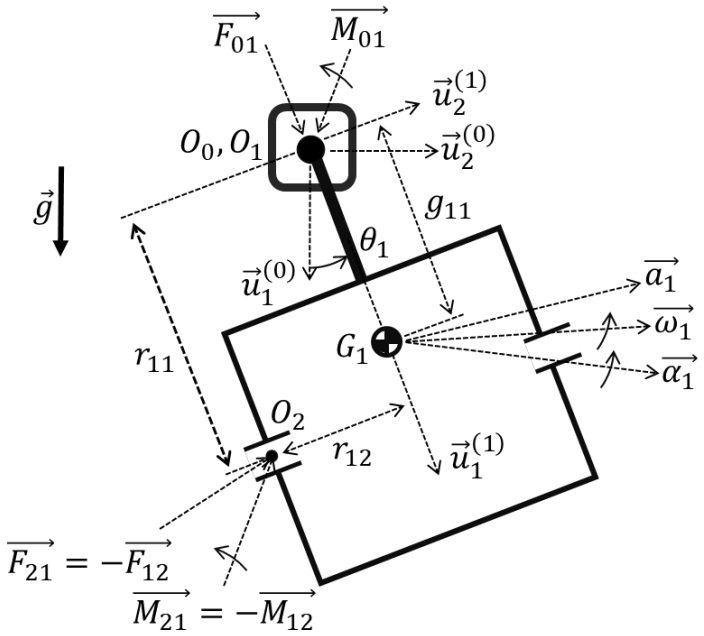

Figure 9. The free-body diagram of the ship

4.1. Kinematic Analyses of the Gyrostabilizer Test System

Initially, for each sub-component, the angular velocity and angular acceleration vectors are computed. Once the angular velocity and angular acceleration analyses have been completed, the linear velocity and linear acceleration of each mass center are determined.

The rotation matrices used are identified with $\hat{R}_i(\theta_j)$ defining a rotation about the $\vec{u}_1$ axis by an amount of θ_j angle. The gyrostabilizer and ship's transformation matrices that define their orientations are formulated by using the formulations shown in Equation 17.

$$\begin{aligned} \hat{C}^{(0,1)} &= \hat{R}_3(\theta_1) \\ \hat{C}^{(1,2)} &= \hat{R}_1\left(-\frac{\pi}{2}\right)\hat{R}_3(\theta_2) \\ \hat{C}^{(2,3)} &= \hat{R}_1\left(-\frac{\pi}{2}\right)\hat{R}_3(\theta_3) \end{aligned} \tag{17}$$

In Equation 17, the $\hat{C}^{(i,j)}$ represents the transformation between frames (j) and (i). Using these matrices, each sub-component's orientation can now be defined relative to the base frame. After defining the transformation matrices, the position level kinematic analyses of each sub-component are defined by using Equation 18.

$$\bar{r}_{O_0G_i} = \bar{r}_{O_0O_i} + \hat{C}^{(0,i)}\bar{r}_{O_iG_i} \tag{18}$$

After the position-level analyses, the angular velocity of each sub-component is analyzed. To accommodate the calculations, a joint space angular velocity for each sub-component is defined as $\dot{\theta}_i$ where $i = 1,2,3$ for the ship, enclosure, and flywheel, respectively. The angular velocity of the subcomponents, measured from the base, is denoted as $\vec{\omega}_{i/0}$. Furthermore, the representation of $\vec{\omega}_{i/i-1} = \dot{\theta}_i\vec{u}_3^{(i)}$ is valid for given free body diagrams. Consequently, the angular velocity of each system component is determined by employing the following Equation 19.

$$\vec{\omega}_{i/0} = \vec{\omega}_{i/i-1} + \vec{\omega}_{i-1/i-2} \dots \vec{\omega}_{1/0} \tag{19}$$

Once the angular velocity of each component has been determined, the angular accelerations are calculated for $\vec{\alpha}_{i/i-1} = \ddot{\theta}_i\vec{u}_3^{(i)}$, where $i = 1,2,3$ for the ship, enclosure, and flywheel, respectively. $\ddot{\theta}_i$ represents the joint space angular acceleration for each component.

$$\vec{\alpha}_{i/0} = \vec{\alpha}_{i-1/0} + \vec{\alpha}_{i/i-1} + \vec{\omega}_{i/0} \times \vec{\omega}_{i/i-1} \tag{20}$$

The velocity level kinematic analyses are performed by using the following Equation 21.

$$\vec{V}_{P/0}^{(d0)} = \vec{V}_{P/A}^{(di)} + \vec{\omega}_{A/0} \times \vec{r}_{P/A} + \vec{V}_{A/0}^{(do)} \tag{21}$$

In Equation 21, $\vec{V}_{P/0}^{(d0)}$ shows the P point linear velocity relative to the metacenter location (O_0) and (do) shows the derivation frame. Similarly, $\vec{V}_{P/A}^{(di)}$ shows the P point linear velocity relative to the A point and shows the derivation frame. In the given system, there is no linear joint, so these terms become zero for all parts. Finally, after defining the linear velocities, the linear acceleration is determined by using the following Equation 22.

$$\begin{aligned}\vec{a}_{\overline{0}}^{(d0)}{}_{P} = \vec{a}_{\overline{A}}^{(di)}{}_{P} + 2\vec{\omega}_{\overline{0}}{}_{i} \times \vec{V}_{\overline{A}}^{(di)}{}_{P} + \vec{\alpha}_{\overline{0}}{}_{i} \times \vec{r}_{\overline{A}}{}_{P} \\ +\vec{\omega}_{i/0} \times \left(\vec{\omega}_{i/0} \times \vec{r}_{P/A}\right) + \vec{a}_{A/0}^{(d0)}\end{aligned} \tag{22}$$

In Equation 22, the linear acceleration of the P point relative to the metacenter location (O_0) is derived in the 0th frame as $\vec{a}_{P/0}^{(d0)}$. Like the velocity level analysis, because of the lack of a linear joint, the $\vec{a}_{P/A}^{(di)}$ term becomes 0 for all equations.

The kinematic analyses of the proposed system are carried out using the provided Equations 17 to 22. The kinematic analyses were conducted by sequentially examining the kinematic properties of each body in the system, beginning with the first body (ship) and concluding with the last body (flywheel). This involved the investigation of the kinematic properties of each pivot and mass center location.

4.2 Dynamic Analyses of the Gyrostabilizer

Once the kinematic analyses of the proposed system have been completed, the dynamic analyses are carried out using calculated acceleration and velocity terms and incorporating the mass properties of each part. The calculations are carried out to define the reaction torques and forces on the connection points (i.e., the joints). In contrast to kinematic analyses, dynamic analyses initiate at the last part and proceed in a step-by-step manner (i.e., a recursive algorithm) until the first part (i.e., the ship). In dynamic analyses, the forces acting at each connection point are calculated using the following Equation 23.

$$m_i \vec{a}_i = \vec{F}_{(i-1)i} + \vec{F}_{(i+1)i} + m_i \vec{g} \tag{23}$$

In Equation 23, the mass of the component is defined as m_i. The forces acting on the system are denoted as $\vec{F}_{(i-1)i}$ and $\vec{F}_{(i+1)i}$. The subscript in the force terms indicates the direction of the force. In response, the magnitude of the force is equal for each body, but its direction changes. The force acting on body i is equal to the force acting on body $i+1$, but in opposite directions: $\vec{F}_{(i+1)i} = -\vec{F}_{i(i+1)}$.

Once the forces acting at the connection points have been defined, the reaction and actuation torques are calculated using Equation 24. Furthermore, the inertial properties must be defined as a second-order tensor, $\check{J}_i$ where $i = 1,2,3$ defined for the ship, enclosure, and flywheel.

$$\begin{aligned} \check{J}_i \cdot \vec{\alpha}_i + \vec{\omega}_i \times \check{J}_i \cdot \vec{\omega}_i = \vec{M}_{(i+1)i} + \vec{M}_{(i-1)i} \\ + \vec{r}_{i(i+1)} \times \vec{F}_{(i+1)i} + \vec{r}_{i(i-1)} \times \vec{F}_{(i-1)i} \end{aligned} \tag{24}$$

Once the dynamic analyses have been completed, the resulting equations are coded in Simulink to verify the accuracy of the analytical solutions. To achieve this, a computer-aided design (CAD) of the scaled-down gyrostabilizer system is developed and later transformed into a MATLAB Multibody model.

5. Gyrostabilizer Test System Design

Once the conceptual design has been finalized, the computer-aided design (CAD) of the ship and the gyrostabilizer system is carried out. The most crucial aspect of the system is to mimic the ship's capacity to roll around the metacentric axis. Figure 10 illustrates the conceptual design and the CAD of the system. Figure 11 illustrates the motion capability of the gyrostabilizer system. Here, the joint-space motions of the ship and enclosure are defined as θ_1 and θ_2, respectively.

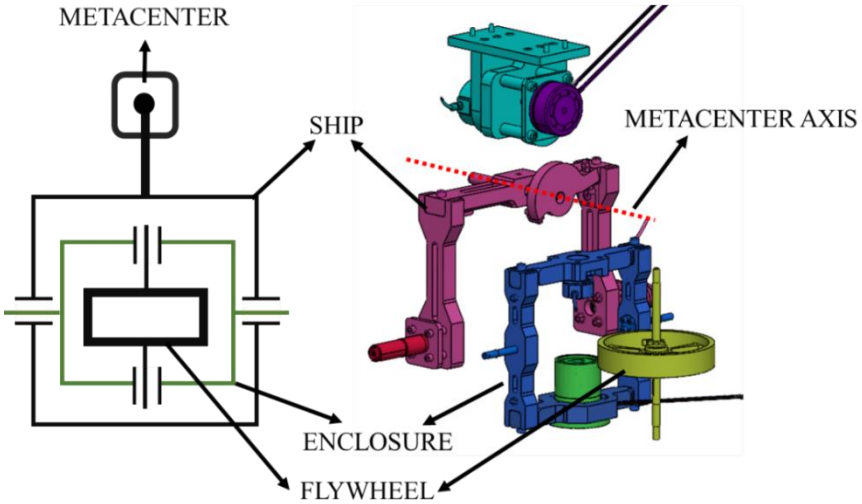

Figure 10. The exploded view of the proposed gyrostabilizer and the ship

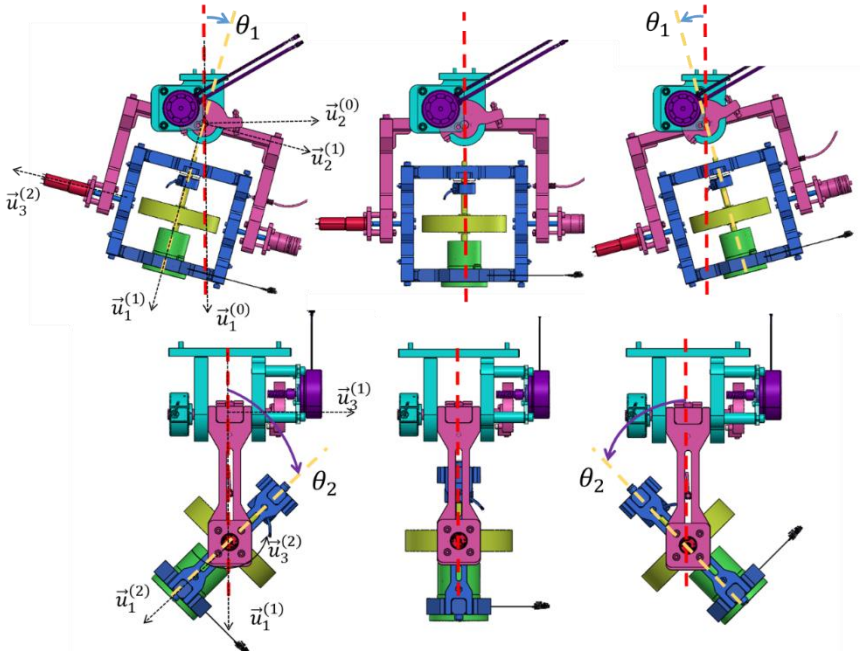

Figure 11. The motion capability of the proposed system

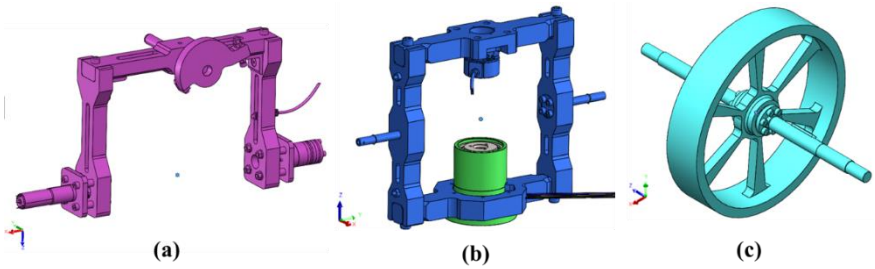

Figure 12. CAD of (a) the ship (b) the enclosure, and the flywheel

Figure 12 illustrates the CAD parts of the proposed system, which include (a) the ship, (b) the enclosure, and (c) the flywheel. The material of the ship part is defined as 6061, the housing is composed of 6061 and 4140, and finally, the flywheel part is composed of ST52 and 4140 steel. The design of the system

has been completed in SolidWorks. The mass and moment of inertia values were obtained via the SolidWorks Mass Properties function. The mass properties of the proposed system are presented in Table 2. The design parameters of the system are tabulated in Table 3.

Table 2. The physical properties of each part of the proposed system

	Mass [kg]	Mass Moment of Inertia [kgm^2]
Ship	$m_1 = 6.931$	$J_1 = \begin{bmatrix} 0.09285 & -0.00021 & -0.00592 \\ -0.00021 & 0.32194 & 0.00477 \\ -0.00592 & 0.00477 & 0.2440 \end{bmatrix}$
Enclosure	$m_2 = 7.016$	$J_2 = \begin{bmatrix} 0.10932 & 0.00042 & 0.00001 \\ 0.00042 & 0.06548 & -0.00001 \\ 0.00001 & -0.00001 & 0.050930 \end{bmatrix}$
Flywheel	$m_3 = 3.43$	$J_3 = \begin{bmatrix} 0.01177 & 0.00000 & 0.00000 \\ 0.00000 & 0.01177 & 0.00000 \\ 0.00000 & 0.00000 & 0.01834 \end{bmatrix}$

Table 3. The design parameters of the proposed system

$g_{11} = 101.23\ [mm]$	$r_{11} = 235[mm]$	$r_{12} = 184.5[mm]$
$g_{23} = 184.5[mm]$	$g_{21} = 0\ [mm]$	$r_{21} = 163.24[mm]$
$r_{23} = 184.5[mm]$	$g_{33} = 163.24[mm]$	

Once the design of the proposed gyrostabilizer and ship system has been completed, it is transferred into MATLAB Simulink as a model composed of Multibody blocks using the Simscape Multibody Link Plugin in SolidWorks. This model is used as the ground truth for validating the kinematic and dynamic analyses.

6. Numerical Model of the Gyrostabilizer System

Figure 13 illustrates the Simulink model of the proposed gyrostabilizer and ship system. In the Simulink model, the parts are connected using revolute joints. These joints are identified as the Wave Imitating Motor, Precession Motor, and Flywheel Motor, respectively. The joint blocks are initially set up to input motion demands. The reason for setting the motion input is to facilitate comparison between the simulation results and the analytical solutions.

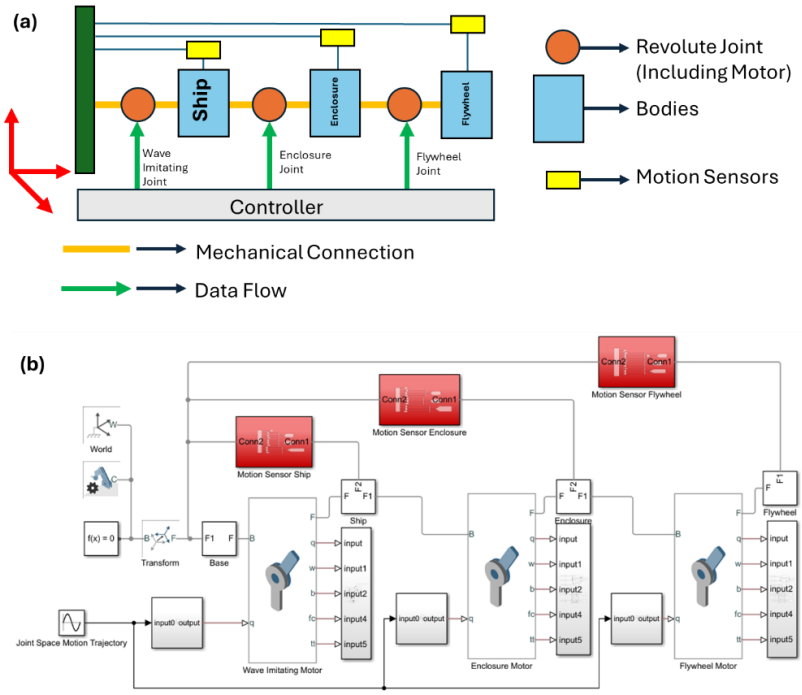

Figure 13. (a) System architecture and flow diagram (b) Fundamental structure of the Simulink model of the proposed system

7. Verification of the Dynamic Model

To facilitate the comparison between the simulation results and the analytical solutions, the kinematic and dynamic equations defined in this paper are coded using MATLAB function blocks. A sine wave with an amplitude of 180˚ and a frequency of 10 [rad/s] is generated. Subsequently, the aforementioned motion input is applied to each joint. Afterwards, the required data, including position, velocity, acceleration, reaction forces, and total torque, are measured through the joint blocks' sensor ports.

The initial step is to investigate the error associated with the kinetic analysis. Figure 14 illustrates the discrepancy between the analytically calculated and measured motion signals.

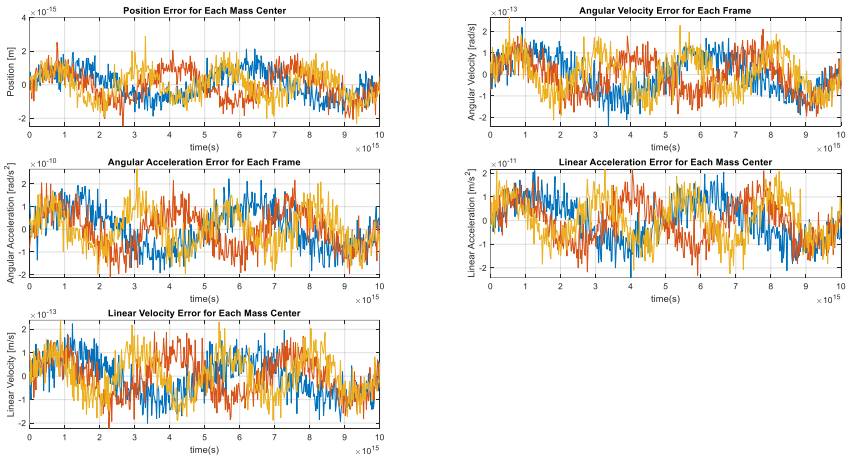

Figure 14. Kinematic analyses error chart for each mass center (G_i) and pivot point (O_i)

When investigating Figure 14, which illustrates the discrepancy between the measured and calculated motion, it is observed that the largest error is observed in the linear acceleration terms, with a value of 10^{-11} $[m/s^2]$. This value is in the numerical error range of the MATLAB simulation. Consequently, the kinematic analyses are evaluated to be accurate.

The next step after validating the kinematic analyses is the validation of the dynamic model. The calculated dynamic forces/moments are compared against the forces and moments acquired from the sensor ports of the Multibody model in MATLAB and presented in Figure 15.

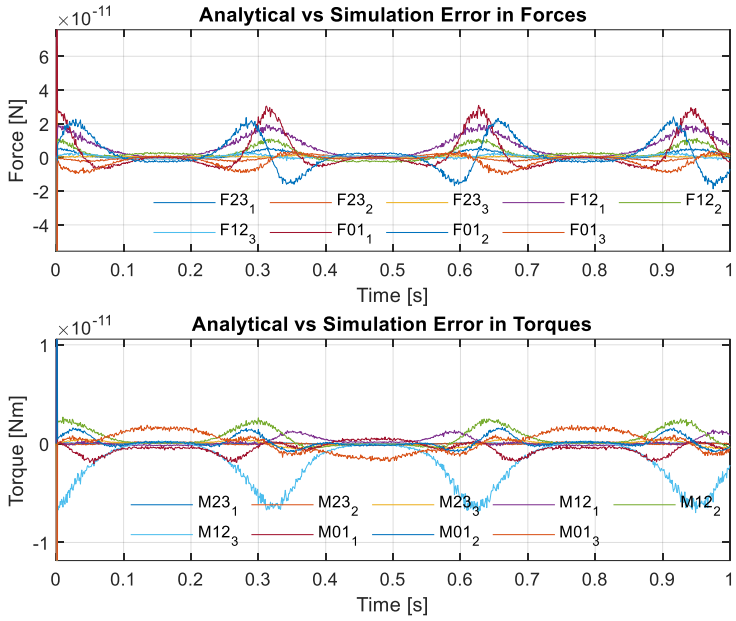

Figure 15. Dynamic analyses error comparison for each pivot point (O_i)

When investigating Figure 15, which illustrates the discrepancy between the calculated and measured dynamic forces/moments, it becomes evident that the error associated with the force analysis falls within the range of $10^{-10}[N]$, while that of the torque level analysis is approximately $10^{-11}[N \cdot m]$. This value is in the numerical error level for MATLAB Multibody simulation. Consequently, dynamic analyses are validated.

The validation of the kinematic and dynamic analyses has enabled the determination of an equation of motion for the scaled-down gyrostabilizer system. This equation of motion can now be used for the control system design. Furthermore, the Simulink file created can be utilized to calculate the reaction forces/moments to accurately design the joint structures.

8. Discussions

Once the dynamic validation has been completed, the motion blocks on the metacenter are removed from the Simulink model. Subsequently, the input of the Wave Imitating Motor joint block is set to Torque Input/Motion Calculated mode. The rationale behind this configuration is to create a back-drivable joint. In this manner, the generated disturbance torques are attenuated by the anti-rolling torque generated by the gyrostabilizer dynamics. After these modifications are issued to the Wave Imitating Motor block, the resulting Simulink model is shown below.

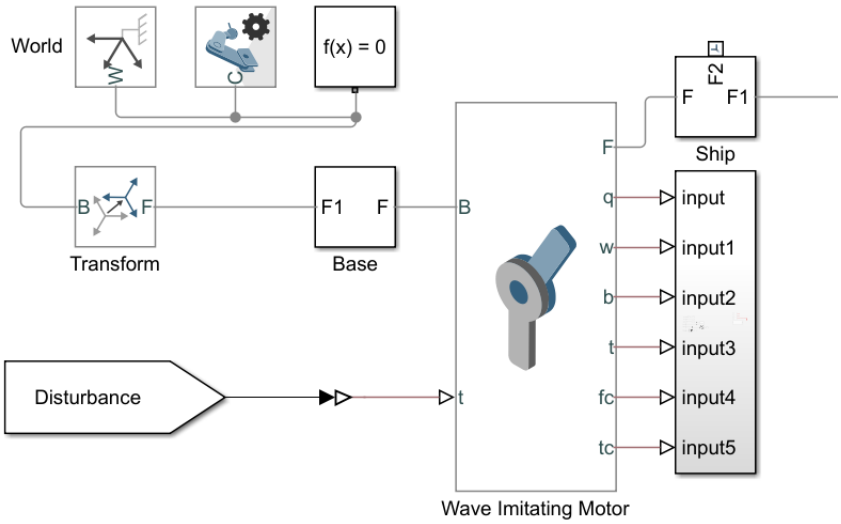

Figure 16. Wave imitating motor block on Simulink model

In the proposed test system, it is planned to utilize a DC motor to generate the precession motion. Consequently, the precession motor block is integrated with a DC motor model generated using the Rotational Multibody Interface. The proposed DC motor model incorporates a number of components, including dampers, inertia, resistors, and inductors, to closely represent the model of a DC motor. Additionally, a gearbox is assembled to the DC motor to amplify the motor's torque. The proposed precession motor model is shown in Figure 17.

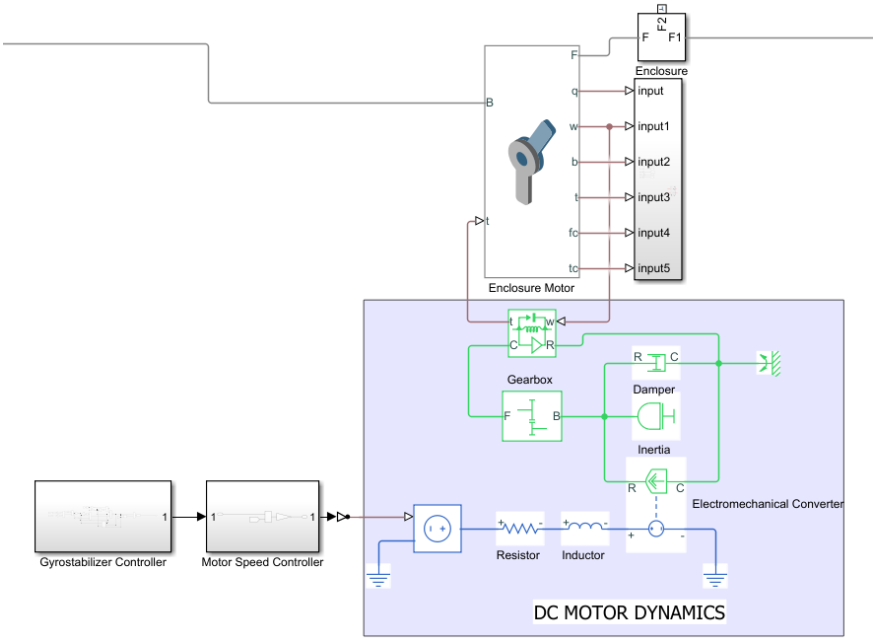

Figure 17. Updated the precession motor joint on the Simulink model

The revised Precession Motor Joint comprises two controllers. The initial controller is the Gyrostabilizer Controller. This controller takes the inputs and generates the precession motion demand. The second controller is the Motor Speed Controller, which takes the precession motion demand as the input. The last controller is the flywheel motion controller, which makes the flywheel reach and maintain the targeted

rotational speed value. These controllers' parameters are tuned as an extension of this study, first in the model and then in the actual test setup.

9. Conclusions

This paper presents the kinematic and dynamic analyses of a scaled-down gyrostabilizer system. Firstly, a conceptual design of the test rig for the gyrostabilizer was performed, which includes the ship. Subsequently, the FBDs of the test rig are sketched individually. The FBDs include the definition of the axes, connection points, mass centers, and body frame axes. Subsequently, the required rotation and transformation matrices are defined. Using this foundation, kinematic analyses are conducted at the position, velocity, and acceleration levels. Then, the kinematic analyses are used to conduct dynamic analyses. Ultimately, the results of the analytical calculations are compared to the results obtained from the generated simulation model for verification purposes. Once the verification process is completed, the Simulink file will be revised to conduct control system studies in the future.

Acknowledgements

This work is supported in part by the Scientific and Technological Research Council of Türkiye via grant number 3220962.

Conflicts of Interest

The author declares that for this article, they have no actual, potential, or perceived conflict of interest.

References

[1]Bergdahl, L. (2009). Wave-induced loads and ship motions. Göteborg: Chalmers University of Technology.
[2]Allied Motion. (2021, October). Boat gyro stabilization system. https://www.alliedmotion.com/applications/commercial-consumer/boat-gyro-stabilization-system/.
[3]Chakraborty, S. (2022, February). Ship stability - understanding curves of static stability. Marine Insight. https://www.marineinsight.com/naval-architecture/ship-stability-understanding-curves-static-stability/.
[4]Dede, M. İ. C. (2024). MATLAB multibody modeli üzerinden robotların kinematik analizi doğrulaması: bir paralel kinematik robot manipülatörü çalışması, FİGES ARGE Dergisi, 36, 24-37.
[5]ITTC. (2002). Final report and recommendations to the 23rd ITTC. Proceedings of the 23rd ITTC, Singapore, 554–59. https://doi.org/10.1007/978-981-10-6946-8_300396.
[6]VEEM Marine. (2021). How gyrostabilizers work [White paper]. https://veemmarine.com/wp-content/uploads/2021/08/Whitepaper-1402-How_Gyrostabilizers_Work-comments.pdf.
[7]Ibrahim, R. A., & Grace, I. M. (2010). Modeling of ship roll dynamics and its coupling with heave and pitch. Mathematical Problems in Engineering, 2010(1), 1-32. https://doi.org/10.1155/2010/934714.
[8]Kornev, N. (2012). Ship dynamics in waves: Ship theory 2 (2nd ed.), Rostock.
[9]Liu, J., Thomas, E., Manuel, L., Griffith, D. T., Ruehl, K. M., & Barone, M. (2018). Integrated system design for a large wind turbine supported on a moored semi-submersible platform. Journal of Marine Science and Engineering, 6(1), Article 9. https://doi.org/10.3390/jmse6010009.
[10]Molland, A. F. (2011). The maritime engineering reference book: A guide to ship design, construction and operation. Elsevier/Butterworth-Heinemann.
[11]O'Hanlon, J. F., & McCauley, M. E. (1973). Motion sickness incidence as a function of the frequency and acceleration of vertical sinusoidal motion (Report No. 1733-1). U.S. Department of Commerce National Technical Information Service. https://doi.org/10.21236/ad0768215
[12]Ölmez, A., & Çakıcı, F. (2022). Theoretical manual of 'YTU Deep' ship motion program. Ocean Engineering, 266(1), Article 112451. https://doi.org/10.1016/j.oceaneng.2022.112451
[13]Pierson, W. J., & Moskowitz, L. (1964). A proposed spectral form for fully developed wind seas based on the similarity theory of S. A. Kitaigorodskii. Journal of Geophysical Research, 69(24), 5181–5190. https://doi.org/10.1029/JZ069i024p05181
[14]Toffoli, A., & Bitner-Gregersen, E. A. (2017). Types of ocean surface waves, wave classification. In J. Carlton, P. Jukes & C. Y. Sang (Eds.), Encyclopedia of Maritime and Offshore Engineering (pp. 1-8). Wiley & Sons. https://doi.org/10.1002/9781118476406.emoe077.

[15]Townsend, N. C., & Shenoi, R. A. (2014). Control strategies for marine gyrostabilizers. IEEE Journal of Oceanic Engineering 39(2), 243-55. https://doi.org/10.1109/joe.2013.2254591.
[16]Townsend, N. C., & Shenoi, R. A. (2011). Gyrostabilizer vehicular technology. Applied Mechanics Reviews 64(1), 1-14. https://doi.org/10.1115/1.4004837.